Dissipative Kerr solitons, breathers and chimera states in coherently driven passive cavities with parabolic potential

Yifan Sun [†],[1,*] Pedro Parra-Rivas,[1,†] Mario Ferraro,[1] Fabio Mangini,[1] Mario Zitelli,[1] Raphael Jauberteau,[1] Francesco Rinaldo Talenti,[1] and Stefan Wabnitz[1,2]

[1] *Department of Information Engineering, Electronics and Telecommunications, Sapienza University of Rome, Via Eudossiana 18, 00184 Rome, Italy*

[2] *CNR-INO, Istituto Nazionale di Ottica, Via Campi Flegrei 34, 80078 Pozzuoli, Italy*

We analyze the stability and dynamics of dissipative Kerr solitons in the presence of a parabolic potential. This potential stabilizes oscillatory and chaotic regimes, favoring the generation of static DKSs. Furthermore, the potential induces the emergence of new dissipative structures, such as asymmetric breathers and chimera-like states. Based on a mode decomposition of these states, we unveil the underlying modal interactions.

Dissipative temporal Kerr soliton (DKS) [1] generation and manipulation have been an emerging topic in photonics over the past decade, since they provide a breakthrough framework for coherent frequency comb generation in chip-scale microresonator platforms [2, 3]. In contrast to conservative systems, where solitons are formed due to a counter-balance between dispersion and nonlinearity, dissipative solitons additionally require an equilibrium between internal dissipation and external energy flow or driving. The dynamics and stability of DKSs have been analyzed in details in the mean-field approximation, where passive Kerr resonators are described by a driven and damped nonlinear Schroedinger model [4, 5]. In this context, a large variety of DKSs emerge in anomalous and normal dispersion regimes [6–8]. As the pump intensity grows larger, DKSs undergo different types of instabilities, leading to complex spatio-temporal dynamics, which can be either periodic (i.e., breathers) or chaotic [9–13].

Spatio-temporal dynamics can be stabilized through high-order effects, such as third-order dispersion, which considerably reduces the extension of unstable parameter regions in favor of static DKSs [14, 15]. Moreover, third- and fourth-order dispersion effects may lead to the appearance of new type localized states, and to the coexistence of bright and dark DKSs [16–18], as it also does the Raman effect [19]. Spatio-temporal instabilities may also be suppressed by the modulation of the intracavity background field. These modulated defects can be induced through the external phase of the driving field [20–25], or by intracavity phase modulation. The latter can be introduced via electro-optical modulators, and it leads to a synthetic dimension [26, 27]. Both methods create an effective periodic potential, which provides an additional degree of freedom for controlling spatio-temporal dynamics and emerging states. Together with the stabilization of chaotic states [28], the potential may lead to the emergence of chimera-like states [26, 29]. Furthermore, a modulated background provides different advantages, such as enhancing the pump-to-soliton conversion efficiency [25], and providing additional deterministic routes for DKSs generation, without undergoing a spatio-temporal chaotic phase [30].

In this letter, we theoretically show that a parabolic potential in time plays a key role on the stability of DKSs and other spatio-temporal dissipative structures emerging in a dispersive Kerr resonator with anomalous dispersion. The parabolic potential approximates a periodic (e.g., sinusoidal) potential around the center of the DKS. Specifically, we find that, for low pump values, the potential stabilizes oscillatory and chaotic dynamics in favor of static DKS. As the pump power grows larger, the potential induces the appearance of asymmetric breathers and *chaoticons*, i.e. chimera-like states, where the background field state coexists with an incoherent spatio-temporal chaotic state. Moreover, chaoticons coexist with single-peak DKSs, and form a hysteresis loop. To support our findings, we carry out a systematic bifurcation analysis, which establishes the connection with the multimodal structure of the potential.

In the mean-field approximation, the coherently driven and phase modulated passive cavity is described by the equation

$$\partial_t A = i\partial_\tau^2 A - iC\tau^2 A + i|A|^2 A - (1+i\delta)A + P, \qquad (1)$$

where $A(\tau, t)$ is the slowly varying envelope of electric field, and τ, t are the fast and slow time, respectively[4]. The term ∂_τ^2 is second-order anomalous chromatic dispersion, δ is the phase detuning, P is the driving pump field amplitude, and the linear loss coefficient, without loss of generality, is fixed to the value of 1. We introduced the parabolic temporal potential $C\tau^2$, where C controls its curvature. Note that such type of potential describes a trap in Bose-Einstein condensates, and a transverse index profile in graded-index multimode fibers [31]. With the usual change of the meaning of the coordinates (e.g., modify time τ with space x), Eq.(1) also describes the spatial dynamics of one-dimensional (e.g., consider slab waveguides) driven nonlinear passive cavities with a graded refractive index [32]. To study the dynamics of Eq. (1), we performed both direct numerical simulations (DNSs) with a pseudo spectral method, and numerical path-continuation of stationary DKS solutions A_s (i.e., $\partial_t A_s = 0$) by using AUTO-07p [33].

Figure 1(a,b) shows the dynamics solutions of Eq.(1) in the absence of the potential ($C = 0$). The temporal evolution ($|A(\tau)|^2$ vs. t) of a chaotic Turing pattern, and its final state are shown in Fig. 1(a) for $(P, \delta) = (2.5, 3)$. Whereas

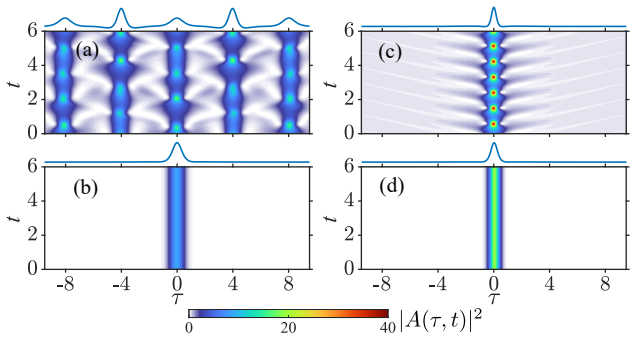

Figure 1. Comparison of solutions without the potential $C = 0$ in (a,c) and with the potential $C = 1$ in (b,d), when the parameters are (a,b) $P = 2.5$, $\delta = 3$ and (c,d) $P = 4.5$, $\delta = 8$.

Fig. 1(b) shows a breather DKS for $(P, \delta) = (4.5, 8)$. For this set of parameters, static DKSs are always unstable [34]. When the potential is introduced ($C = 1$) [see Figs. 1(c,d)], these dynamics are stabilized, leading to stationary DKSs.

In order to understand the mechanism for this stabilization, we performed a bifurcation analysis of the DKSs, with and without a temporal potential. These results are illustrated in Fig. 2, using $I_{center} \equiv |A(0)|^2$ vs. δ. DKS bifurcation diagrams, either in the absence [see Fig. 2(a,c)] or in the presence [see Fig. 2(b,d)] of the potential; we set $P = 2.5$ [Fig. 2(a,b)] or $P = 4.5$ [Fig. 2(c,d)]. These diagrams were computed by utilizing path-continuation algorithms for stationary solutions, and DNSs for breathers and chaotic solutions.

Figure 2(a) shows the bifurcation diagram in the absence of potential, with $P = 2.5$. The blue curve corresponds to the continuous-wave (CW) state of Eq.(1). The CW state is stable until the saddle-node (SN) bifurcation SN_h^l, where it becomes unstable [see dashed blue lines]. The DKS bifurcates from SN_h^l with a small amplitude, and it remains unstable [see orange dashed lines] [7]. By increasing δ, the DKS eventually stabilizes at SN^r, and it retains stability until reaching SN^l [see solid red line]. These solitons have a non-zero background (corresponding to the CW state), and their localized profile can be approximated by a sech-shape [1]. When decreasing δ below SN_h^l, the DKS background becomes unstable, leading to chaotic Turing pattern states, such as in the example shown in Fig. 1 for $(\delta, P) = (3, 2.5)$. The peak intensity values of these states are plotted by gray dots in Fig. 2(a).

This scenario drastically changes in the presence of the parabolic potential [see Fig. 2(b)]. Now, the CW state diagram merges with the solution branches corresponding to the DKS, leading to the single curve of Fig. 2(b). Each branch on this curve corresponds to DKSs, as depicted in Fig. 2(i)-(iii); these branches are interconnected through the SN bifurcations $\mathrm{SN}_p^{l,r}$.

The S_3 state plotted in Fig. 2(i) is a small-amplitude localized pulse, which corresponds to the deformation of the CW state, owing to the presence of the potential. This state extends until SN_p^l, where it connects to the unstable state

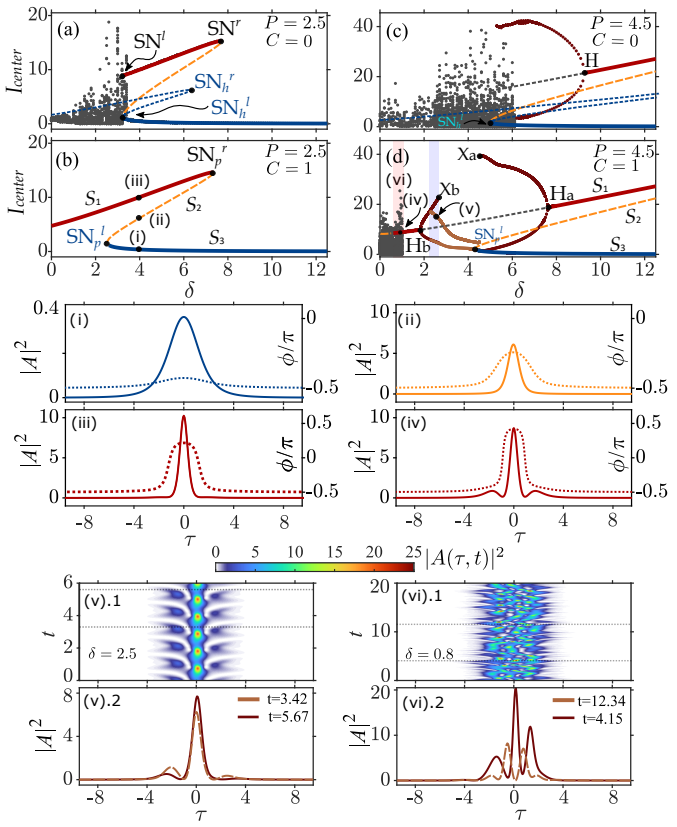

Figure 2. Bifurcation diagrams showing I_{center} vs. δ for $(P, C) = (2.5, 0)$ in (a), $(P, C) = (2.5, 1)$ in (b), $(P, C) = (4.5, 0)$ in (c), and $(P, C) = (4.5, 1)$in (d). Panels (i)-(iii) show the intensity $|A|^2$ (solid line) and phase ϕ (dashed line) of the three DKS solutions S_1, S_2 and S_3, corresponding to the curve in panel (b) for $(\delta, P, C) = (4, 2.5, 1)$; panel (iv) corresponds the DKS solution in panel (d) for $(\delta, P, C) = (4, 0.8, 1)$. Panel (v).1 represents the evolution of a τ-asymmetric state ($(\delta, P, C) = (4, 2.5, 1)$), and panel (vi).1 shows a chaoticon ($(\delta, P, C) = (4, 0.8, 1)$). The corresponding field powers at different slow times are in panels (v).2 and (vi).2, respectively [See Visualization I and II].

S_2 [see Fig. 2(ii)]. At SN_p^r, the latter leads to S_1, which is a stable localized pulse [see Fig. 2(iii)]. S_1 represents a deformation of the DKS with $C = 0$, sitting on the primary state S_3. Thus, S_1 is asymptotically connected to a zero intensity background. For $C = 1$, S_1 extends until $\delta = 0$ and it is stable, in contrast with the $C = 0$ case. Between SN_p^l and SN_p^r, S_1 and S_3 coexist for the same range of parameters, and are both stable. DKS bistability is a feature of Eq.(1), which is absent with $C = 0$. The localized states S_1 and S_3 can be easily excited by a Gaussian function of the form $A(\tau) = h \exp\left(-(\tau/r)^2/2\right)$, with h and r taking different values.

As we have anticipated with Fig. 1, the stabilization of the dynamics of solutions to Eq.(1) occurs for different values of P. To support this discovery, we computed the bifurcation diagram associated with a single-peak soliton for $P = 4.5$, with and without the potential. This situation is depicted in Fig. 2(c,d). Figure 2(c) shows the bifur-

cation diagram for $C = 0$. By increasing P, the role of nonlinearity grows larger, which further tilts the resonance [see the blue lines]. The DKS solution branches preserve the morphology depicted in Fig. 2(a), although now their range of existence has increased. In this regime, the top DKSs branch undergoes a Hopf bifurcation (H), where the soliton becomes unstable in favor of breathing states. The minimal and maximal value of I_{center} of these breathers are plotted by means of red dots. These breather states are similar to that depicted in Fig. 1(c), and their oscillation amplitude grows larger with decreasing values of δ. Eventually, when SN_h^l is crossed, the stable CW state disappears, and spatio-temporal chaos (STC) develops. Note that STC extends their region over SN_h^l, and coexists with DKSs or breathers [see Fig. 2(a,c)].

For $C = 1$ [see Fig. 2(d)], STC is suppressed by the potential, in favor of either static DKS or regular oscillatory states. The DKS S_1 enlarges its stability region, which now extends to H_a, where $\delta_{\mathrm{H}_a} \ll \delta_{\mathrm{H}}$. Once H_a is crossed, a τ-symmetric breather arises supercritically, and it increases its oscillation amplitude with decreasing values of δ. Eventually, this stable breather disappears, possibly in a fold of cycles at X_a. By decreasing δ below this point, the system develops τ-asymmetric breathers, such as the one which is depicted in Fig. 2(v) for $(\delta, P) = (2.5, 4.5)$ [See Visualization I]. A special feature of these states is the different evolution of their leading and trailing tails. The extrema of these states, at $\tau = 0$, are depicted by using brown dots in Fig. 2(d). Decreasing δ further, the asymmetric breather branch meets with a symmetric one [see dark red branch] and disappears. On the right, the latter persists until reaching X_b. On the left, the τ-symmetric breather decreases its amplitude, until it dies out at the Hopf bifurcation H_b. Note the presence of a bistability region between the symmetric and asymmetric breathers [see the light blue shadowed area in Fig. 2(d)]. For $\delta < \delta_{\mathrm{H}_b}$, DKSs exist [such as the one shown in Fig. 2(iv).], although they lose stability once more around $\delta \approx 0.5$. After this, the system evolves into a very complex spatio-temporal state, such as the one shown in Fig. 2(vi). This state consists of a portion of STC which is localized around the center of the temporal domain owing to the presence of the potential which acts as a trap, thus confining the STCs. This type of state was named chaoticon by Vershueren *et al.* [35], although it is also known as chimera state in other works [26, 29]. The chaoticon coexists with DKSs [see the pink shadowed area in Fig. 2(d)], as in the cases with the same parameters which depicted in Fig. 2(iv) and Fig. 2(vi) [See Visualization II].

The previously described states can be analyzed in terms of a mode decomposition method. The parabolic potential introduces boundary conditions for the fields, which translate in a finite number of eigenmodes. Therefore, solutions of Eq.(1) in Fig. 2 can be decomposed and analyzed in terms of nonlinear eigenmodes. For the sake of simplicity, here we perform this analysis by using the linear eigenmodes associated with the equation

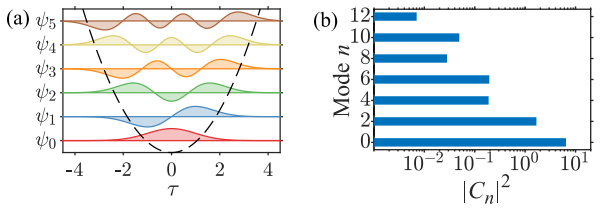

Figure 3. (a) shows the first six HG linear modes $\psi_0, \cdots, \psi_5$ of Eq.(1) and of the parabolic potential [see dashed line], for comparison. (b) illustrates the mode energy distribution associated with the S_1 DKS shown in Fig. 2(iii) for $(\delta, P) = (4, 2.5)$, where $|C_n|^2$ represents the energy of the mode n.

$$\partial_t A = i\partial_\tau^2 A - iC\tau^2 A, \tag{2}$$

which also describes a quantum mechanical harmonic oscillator. Note that a similar equation was also used for describing the dynamics of mode-locked nanolasers [36, 37]. As it is well-known, the eigenmodes of Eq. (2) are the Hermite-Gaussian (HG) family. The lowest order six modes are plotted in Fig. 3(a). The neglected terms in Eq. (2), compared with Eq. (1), can be considered as small perturbations. The field envelope $A(\tau, t)$ can be written as a linear superposition of HG modes $\psi_n(\tau)$ with equally spaced frequencies $\sqrt{2C}(n + 1/2)$, $A(\tau, t) = \sum_{n=0}^{N} C_n(t)\psi_n(\tau)$, with N being the total number of modes considered in the analysis. The mode coefficients are computed by projecting any state solution on the linear modes, and read as $C_n(t) = \int_{-\infty}^{\infty} A(\tau, t)\psi_n(\tau)\mathrm{d}\tau = |C_n(t)| \exp\{\mathrm{i}\phi_n(t)\}$, where $|C_n(t)|^2$ represents the energy of mode n at time t, and $\phi_n(t)$ is its phase. In Fig. 3(b), we plot the mode energy $|C_n|^2$ distribution associated with the DKS state S_1 in Fig. 2(iii). Note that the energies of asymmetric modes $(n = 1, 3, 5, \cdots)$ are zero, because the state has a symmetric temporal distribution. S_2 and S_3 have a similar mode distribution [not shown here].

The bifurcation structure shown in Fig. 2(d) ($P = 4.5$) can be revisited by projecting the different DKS branches on HG modes. This projection is depicted in Fig. 4(a), where we plot the mode energy $|C_0|^2$ and $|C_2|^2$ vs. δ. Following this diagram, we can see how the $\psi_{0,2}$-mode composition varies along the solution branches S_1, S_2 and S_3.

More interestingly, in Fig. 4(b) we show the phase difference between the two modes ψ_0 and ψ_2 along the bifurcation diagrams of Fig. 4(a). This diagram shows that the phase difference between adjacent symmetric modes is $-\pi$ in S_1 [other higher-order modes are not shown here], which means that these modes are locked in anti-phase, in contrast with the in-phase mode locking that occurs for S_3 states. Whereas the unstable states S_2 undergo large phase changes between the two modes. The bifurcation structure is preserved, and one can appreciate the positions of $\mathrm{H}_{a,b}$ and $\mathrm{SN}_p^{l,r}$.

We have analyzed in more detail the variation of the mode composition of stable states S_3 [see Figs. 4(c)] and

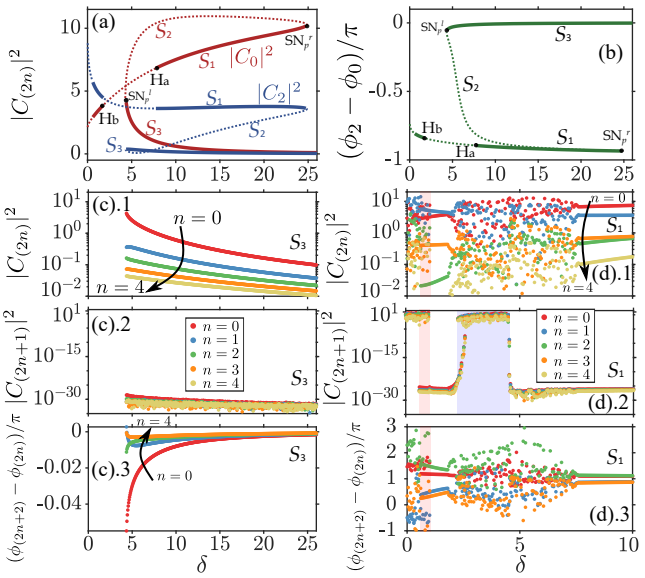

Figure 4. Mode decomposition of the solutions in Fig. 2(d). Mode energies $|C_0|^2$, $|C_2|^2$ in (a) and their phase difference in (b) as a function of δ, where solid (dashed) lines represent stable (unstable) solutions. Three panels in (c) plot even mode energies $|C_{(2n)}|^2$, odd mode energies $|C_{(2n+1)}|^2$, and phase difference $(\phi_{(2n+2)} - \phi_{(2n)})/\pi$ vs. δ, for S_3 solutions in Fig. 2(d). The same quantities of the solutions S_1 of Fig. 2(d) are shown in three panels in (d). The regime where chaoticon coexists with DKSs (the regime of asymmetric breathers) is represented by the pink (blue) shadowed area.

S_1 [see Figs. 4(d)], as function of δ. For S_3, the energy of the symmetric modes (i.e., $|C_{(2n)}|^2$, $n \in \mathbb{N}$) increases with decreasing δ, until reaching SN_p^l. Energy in each mode decreases with increasing δ, and the power fraction of higher-order modes grows larger. This leads to a temporal broadening of S_3 states, owing to the contribution of higher-order modes. In contrast, the contribution of asymmetric modes (i.e., $|C_{(2n+1)}|^2$) remains close to zero [see Fig. 4(c).2]. Figure 4(c).3, illustrates how the phase difference between adjacent even modes $(\phi_{(2n+2)} - \phi_{(2n)})/\pi$ approaches zero when δ increases. This shows that stronger phase locking occurs for these modes with increasing δ.

Figures 4(d) illustrate the mode decomposition of S_1: here we may highlight three main aspects. First, in the breather regimes between $1.8 < \delta < 7.5$, even mode powers [see Fig. 4(d).1] and phase differences [see Fig. 4(d).3] fluctuate. Second, in the regions of asymmetric breathers and chaoticons, the power of odd modes becomes very high [see Fig. 4(d).2], which give their contributions to the asymmetric and chaotic evolutions. Finally, for S_1 the mode energies increase, in contrast to S_3, for which they decrease.

In summary, by applying a bifurcation analysis, we revealed the emergence and stability of dissipative states for a driven passive nonlinear cavity with a parabolic potential. The potential may stabilize complex spatio-temporal dynamics in favor of static DKSs, and leads to the coexistence of high and low amplitude DKSs. A particular feature of this system is that asymmetric breathers and chimera-like states (i.e., a chaoticons) may arise. The latter, consist of localized spatio-temporal chaos, and appear due potential trapping. By a modal decomposition analysis we have shown that these states emerge from interactions of asymmetric modes. The simple parabolic potential captures the essential dynamics introduced by synchronous phase modulation [26, 29], while providing useful physical insight based on a linear mode decomposition.

ACKNOWLEDGMENTS

This work was supported by European Research Council (740355), Marie Sklodowska-Curie Actions (101064614, 101023717), Ministero dell'Istruzione, dell'Universita e della Ricerca (R18SPB8227), Sapienza University of Rome (AR22117A7B01A2EB, AR22117A8AFEF609, RG12117A84DA7437)

* yifan.sun@uniroma1.it
† These authors have contributed equally.

[1] S. Wabnitz, Opt. Lett. **18**, 601 (1993).
[2] T. Herr, V. Brasch, J. D. Jost, C. Y. Wang, N. M. Kondratiev, M. L. Gorodetsky, and T. J. Kippenberg, Nature Photonics **8**, 145 (2014).
[3] A. Pasquazi, M. Peccianti, L. Razzari, D. J. Moss, S. Coen, M. Erkintalo, Y. K. Chembo, T. Hansson, S. Wabnitz, P. Del'Haye, X. Xue, A. M. Weiner, and R. Morandotti, Physics Reports **729**, 1 (2018).
[4] M. Haelterman, S. Trillo, and S. Wabnitz, Optics Communications **91**, 401 (1992).
[5] Y. K. Chembo, D. Gomila, M. Tlidi, and C. R. Menyuk, The European Physical Journal D **71**, 299 (2017).
[6] P. Parra-Rivas, E. Knobloch, D. Gomila, and L. Gelens, Physical Review A **93**, 063839 (2016).
[7] P. Parra-Rivas, D. Gomila, L. Gelens, and E. Knobloch, Physical Review E **97**, 042204 (2018).
[8] P. Parra-Rivas, E. Knobloch, L. Gelens, and D. Gomila, IMA Journal of Applied Mathematics **86**, 856 (2021).
[9] F. Leo, S. Coen, P. Kockaert, S.-P. Gorza, P. Emplit, and M. Haelterman, Nature Photonics **4**, 471 (2010).
[10] M. Anderson, F. Leo, S. Coen, M. Erkintalo, and S. G. Murdoch, Optica **3**, 1071 (2016).
[11] Z. Liu, M. Ouali, S. Coulibaly, M. G. Clerc, M. Taki, and M. Tlidi, Optics Letters **42**, 1063 (2017).
[12] E. Lucas, M. Karpov, H. Guo, M. L. Gorodetsky, and T. J. Kippenberg, Nature Communications **8**, 736 (2017).
[13] C. Bao, Y. Xuan, C. Wang, A. Fülöp, D. E. Leaird, V. Torres-Company, M. Qi, and A. M. Weiner, Physical Review Letters **121**, 257401 (2018).
[14] C. Milián and D. V. Skryabin, Optics Express **22**, 3732 (2014).
[15] P. Parra-Rivas, D. Gomila, F. Leo, S. Coen, and L. Gelens, Optics Letters **39**, 2971 (2014).
[16] M. Tlidi and L. Gelens, Optics Letters **35**, 306 (2010).
[17] P. Parra-Rivas, D. Gomila, and L. Gelens, Physical Review A **95**, 053863 (2017).

[18] Z. Li, Y. Xu, S. Coen, S. G. Murdoch, and M. Erkintalo, Optica **7**, 1195 (2020).
[19] P. Parra-Rivas, S. Coulibaly, M. Clerc, and M. Tlidi, Physical Review A **103**, 013507 (2021).
[20] S. Wabnitz, J. Opt. Soc. Am. B **13**, 2739 (1996).
[21] J. K. Jang, M. Erkintalo, S. Coen, and S. G. Murdoch, Nature Communications **6**, 10.1038/ncomms8370 (2015).
[22] D. C. Cole, J. R. Stone, M. Erkintalo, K. Y. Yang, X. Yi, K. J. Vahala, and S. B. Papp, Optica **5**, 1304 (2018).
[23] I. Hendry, B. Garbin, S. G. Murdoch, S. Coen, and M. Erkintalo, Physical Review A **100**, 10.1103/PhysRevA.100.023829 (2019).
[24] F. R. Talenti, T. Hansson, and S. Wabnitz, *Advanced Photonics Congress 2020*, Advanced Photonics Congress 2020 , JTu2D.4 (2020).
[25] M. Erkintalo, S. G. Murdoch, and S. Coen, Journal of the Royal Society of New Zealand **52**, 149 (2022).
[26] A. K. Tusnin, A. M. Tikan, and T. J. Kippenberg, Physical Review A **102**, 10.1103/PhysRevA.102.023518 (2020).
[27] N. Englebert, N. Goldman, M. Erkintalo, N. Mostaan, S.-P. Gorza, F. Leo, and J. Fatome, arXiv preprint arXiv:2112.10756 (2021).
[28] V. E. Lobanov, G. V. Lihachev, N. G. Pavlov, A. V. Cherenkov, T. J. Kippenberg, and M. L. Gorodetsky, Optics Express **24**, 27382 (2016).
[29] A. U. Nielsen, Y. Xu, M. Ferré, M. G. Clerc, S. Coen, S. G. Murdoch, and M. Erkintalo, arXiv preprint arXiv:1910.11329 (2019).
[30] H. Taheri, A. A. Eftekhar, K. Wiesenfeld, and A. Adibi, IEEE Photonics Journal **7**, 10.1109/JPHOT.2015.2416121 (2015).
[31] K. Krupa, A. Tonello, A. Barthélémy, T. Mansuryan, V. Couderc, G. Millot, P. Grelu, D. Modotto, S. A. Babin, and S. Wabnitz, APL Photonics **4**, 110901 (2019).
[32] M. Haelterman, S. Trillo, and S. Wabnitz, Optics Communications **93**, 343 (1992).
[33] E. J. Doedel, B. E. Oldeman, A. R. Champneys, F. Dercole, T. Fairgrieve, Y. A. Kuznetsov, R. Paffenroth, B. Sandstede, X. Wang, and C. Zhang, Department of Computer Science, Concordia University, Montreal (2007).
[34] F. Leo, L. Gelens, P. Emplit, M. Haelterman, and S. Coen, Optics Express **21**, 9180 (2013).
[35] N. Verschueren, U. Bortolozzo, M. G. Clerc, and S. Residori, Philosophical Transactions of the Royal Society A: Mathematical, Physical and Engineering Sciences **372**, 20140011 (2014), publisher: Royal Society.
[36] Y. Sun, S. Combrié, F. Bretenaker, and A. D. Rossi, Physical Review Letters **123**, 233901 (2019).
[37] Y. Sun, S. Combrié, A. D. Rossi, and F. Bretenaker, Physical Review A **102**, 043503 (2020).